Highlights

High-resolution ILW outflow boundary treatment for the Navier–Stokes equations

Luciano K. Araki,Rafael B. de R. Borges,Nicholas Dicati P. da Silva,Chi-Wang Shu

- The ILW outflow boundary treatment behave similarly to the far-field strategy
- The domain size can be reduced significantly
- Dimensional flows can be solved with the employed methods
- High-resolution viscous terms discretization and ILW are promising in solving engineering problems

High-resolution ILW outflow boundary treatment for the Navier–Stokes equations

Luciano K. Araki[a], Rafael B. de R. Borges[b], Nicholas Dicati P. da Silva[c] and Chi-Wang Shu[d,1]

[a]*Federal University of Paraná, Curitiba, Paraná, Brazil*
[b]*Rio de Janeiro State University, Rio de Janeiro, Rio de Janeiro, Brazil*
[c]*Maringá State University, Maringá, Paraná, Brazil*
[d]*Brown University, Providence, Rhode Island, USA*

ARTICLE INFO

Keywords:
Compressible fluid flow
High-order and -resolution methods
ILW boundary treatment

ABSTRACT

WENO schemes have high-resolution and great capability of capturing unsteady and non-linear phenomena. These phenomena occur in elaborated flows, such as cascade and external aerodynamic flows. Thus, high-resolution methods play an important role in modern CFD. Easiness and effectiveness are reached when implementing these methods in rectangular meshes. However, one has the non-boundary-conforming issue. To overcome it the ILW procedure can be employed. We showed that the ILW has a similar behavior to the far-field boundary treatment. Then, we proposed and tested a new ILW outflow boundary treatment and an WENO-type extrapolation. We employed the finite difference method with the positivity-preserving Lax–Friedrichs splitting, high-resolution viscous terms discretization, multi-resolution WENO scheme, and third-order strong stability preserving Runge–Kutta time discretization. We tested the proposed methods in a smooth test case, supersonic flow past a cylinder, NACA 0012 nitrogen flows with 0 and 12 ° angle of attack, and a NACA 9520 cascade airflow. The proposed methods have high order and resolution, allowed domain size reduction, and captured unsteady and non-linear phenomena. Although preliminary, the NACA 0012 and 9520 flows showed the methods are promising. Common issues with other methods are also reported and further improvements are needed. For example, local mesh refinement, high-order wall boundary treatment, and turbulence modeling.

1. Introduction

High-order and -resolution boundary treatments for CFD are an active research field. Among them, we focus on non-boundary-conforming grid methods, i.e., to handle the cut cell problem [21, 34, 16, 5]. Their advantage is the use of rectangular meshes, whose structure and generation are simpler. Furthermore, high-order and -resolution interior schemes are easily implemented on structured meshes. Among the non-boundary-conforming grid methods, we have the Inverse Lax-Wendroff (ILW) procedure. Its recent foundation started with the works of [26], [27], and [28] for conservation laws and was expanded to viscous flows in [15]. Improvements and modifications were made in [16], [6], and [5]. Several tests were carried on in many different CFD problems. Still, one can perform a few improvements and tests, e.g., outflow boundaries and high-magnitude flow properties.

For the Euler equations, well-established and well-tested strategies are available. In [20], the authors established the number and type of boundary conditions for the Navier–Stokes equations. In [15], the authors separated convective and diffusive boundary requirements. This elegant strategy also eases the boundary treatment. Therefore, before fulfilling the boundary requirements, we must identify its type. For example, a common boundary type is a solid wall. Strategies for the Euler equations and Navier–Stokes are available in [16], [6], and [5]. Another common type is the outflow boundary in external flows, which is usually handled with far-field strategies.

Without proper handling, the outflow boundary condition can produce an unphysical behavior. This can contaminate the whole computational domain or cause the solution to blow up. For example, in a supersonic external flow modelled by the Euler equations. If one extrapolates all the characteristic variables using high-order methods, it may cause the flow to over-expand and the solution can blow up, even if the solution at the outflow is supersonic. Marching from the initial guess to the steady solution can generate subsonic regions. The subsonic regions will need to cross the outflow boundary, causing overexpansion. For this purpose, far-field boundary conditions are a class of popular and robust strategies [3, 33, 29, 9, 14, 25, 12].

A common building block for far-field strategies is the Riemann invariants (or variables). They are also found in exact and approximate Riemann solvers. For example, consider the following Riemann invariants [29, 14, 12]

$$Ri^{\pm} = \hat{u} \pm \frac{2a}{\gamma - 1}, \tag{1}$$

where $\hat{u}$ is the normal velocity to the boundary, a is the speed of sound, and γ is the specific heat ratio.

Consider the Riemann problem for the Euler equations. The Riemann invariants of (1) are constant between rarefaction waves and the star region [30]. That is sufficient for

---

*Corresponding author
Email address: `ndicati@gmail.com` (N.D.P. da Silva)
ORCID(s): 0000-0003-0130-739X (L.K. Araki); 0000-0002-2576-8118 (R.B.d.R. Borges); 0000-0002-5808-3932 (N.D.P. da Silva)

[1] The research of C.-W. Shu is partly supported by AFOSR grant FA9550-20-1-0055 and NSF grant DMS-2010107.

testing exact Riemann solvers as a building block. However, the computational cost may be limiting. The exact Riemann solver assesses the type and wave direction. Approximate solvers or the characteristic boundary can also assess them. The latter is already incorporated in the ILW procedure.

The boundary treatment success also depends on the extrapolation and variable types. For example, [16] and [5] proposed the approximation of conservative variables, fluxes, and viscous terms. If the problem is nondimensionalized or one applies a normalization, working with those variables will not be a problem. However, for dimensional problems the magnitude of, e.g., pressure will be high. This leads to a problem when performing one- or two-dimensional approximations. For the extrapolation, one common drawback of the WENO-type extrapolation is the dependency of the non-linear weights on the smaller substencils smoothness indicators [26, 16].

The objective of this work is to present a strategy for imposing high-order and -resolution outflow ILW boundary treatment for the Navier–Stokes equations, suitable for high-magnitude variables. To do so, we split our effort into two situations. First, we show the similarities between the exact Riemann solver and a far-field strategy. Then, we extrapolate only characteristic variables in the ILW procedure. We also propose a new WENO-type extrapolation with more generic non-linear weights. We test the proposed **strategies** in a smooth problem, supersonic flow past a cylinder, subsonic flows past a NACA 0012 airfoil, and a NACA 9520 cascade flow. We construct rectangular meshes and employ the finite difference method with the positivity-preserving Lax–Friedrichs splitting [35], high-resolution viscous terms discretization [5], fifth-order multi-resolution WENO [36], and the third-order strong stability preserving Runge–Kutta [23].

2. A comparison between the far-field boundary condition and the exact Riemann solver

In this work, we are interested in the Navier–Stokes equations

$$\boldsymbol{U}_t + \boldsymbol{F}(\boldsymbol{U})_x + \boldsymbol{G}(\boldsymbol{U})_y = \boldsymbol{S_1}_x + \boldsymbol{S_2}_y + \boldsymbol{S}(\boldsymbol{U}), \tag{2}$$

where

$$\boldsymbol{U} = \begin{bmatrix} \rho \\ \rho u \\ \rho v \\ E \end{bmatrix}, \quad \boldsymbol{F}(\boldsymbol{U}) = \begin{bmatrix} \rho u \\ \rho u^2 + p \\ \rho u v \\ u(E+p) \end{bmatrix}, \quad \boldsymbol{G}(\boldsymbol{U}) = \begin{bmatrix} \rho v \\ \rho u v \\ \rho v^2 + p \\ v(E+p) \end{bmatrix}, \tag{3}$$

$$\boldsymbol{S_1} = \begin{bmatrix} 0 \\ \tau_{xx} \\ \tau_{xy} \\ u\tau_{xx} + v\tau_{xy} + \dfrac{\mu}{Pr(\gamma-1)}\dfrac{\partial(a^2)}{\partial x} \end{bmatrix}, \tag{4}$$

$$\boldsymbol{S_2} = \begin{bmatrix} 0 \\ \tau_{xy} \\ \tau_{yy} \\ u\tau_{xy} + v\tau_{yy} + \dfrac{\mu}{Pr(\gamma-1)}\dfrac{\partial(a^2)}{\partial y} \end{bmatrix}, \tag{5}$$

where the source term $\boldsymbol{S}(\boldsymbol{U})$ depends on the problem, and ρ, u, v, and p are the density, x and y velocities, and pressure. E, $\boldsymbol{\tau}$, and a are the the total energy per unit of volume, viscous tensor, and speed of sound, given as

$$E = \frac{p}{\gamma-1} + \frac{\rho}{2}(u^2+v^2), \;\; \tau_{xx} = \mu\left(\frac{4}{3}\frac{\partial u}{\partial x} - \frac{2}{3}\frac{\partial v}{\partial y}\right), \tag{6}$$

$$\tau_{xy} = \mu\left(\frac{\partial u}{\partial y} + \frac{\partial v}{\partial x}\right), \;\; \tau_{yy} = \mu\left(\frac{4}{3}\frac{\partial v}{\partial y} - \frac{2}{3}\frac{\partial u}{\partial x}\right), \tag{7}$$

$$a = \sqrt{\frac{\gamma p}{\rho}}, \tag{8}$$

where μ and Pr are the absolute viscosity and the Prandtl number.

For the inviscid flux and viscous term discretization, time integration, and other details, the reader is referred to [23], [35], [36], and [5].

Our goal is to solve a similar supersonic flow past a cylinder as in [5]. For simplicity, we use the lower-order characteristic boundary condition at the left and upper domain boundaries. The average state is $\boldsymbol{U}_{\text{avg}} = (\boldsymbol{U}_{\text{near}} + \boldsymbol{U}_{\infty})/2$, where near means the nearest point to the boundary and ∞ means free-stream property. Then, we do a local characteristic decomposition. That is, we compute the eigenvalues and left and right eigenvectors. For the left boundary, the inflow is supersonic and we impose all four characteristic variables:

$$\boldsymbol{V}_{\infty} = \boldsymbol{L}(\boldsymbol{U}_{\text{avg}})\boldsymbol{U}_{\infty}, \tag{9}$$

$$\boldsymbol{V}_{i,j} = \boldsymbol{V}_{\infty}, \tag{10}$$

where $i = -2, \dots, 0$ are the ghost points for a fixed j. Then, we transform back to the conservative variables

$$\boldsymbol{U}_{i,j} = \boldsymbol{R}(\boldsymbol{U}_{\text{avg}})\boldsymbol{V}_{i,j}. \tag{11}$$

We can approximate $v \approx 0$, since the oblique shock does not cross the upper boundary. Therefore,

$$(V_m)_{i,j} = (V_{\text{near}})_m, \quad m = 2, 3, 4, \tag{12}$$

$$(V_1)_{i,j} = (V_{\infty})_1, \tag{13}$$

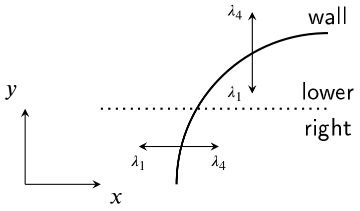

(a) Left side of the cylinder.

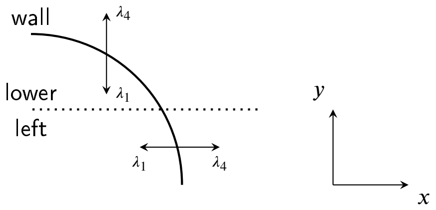

(b) Right side of the cylinder.

Figure 1: Eigenvalues and wall boundary configuration.

where $j = N_y + 1, \dots, N_y + 3$ for a fixed i. Then, we transform back.

One should notice that we only considered the convective part. This provides a simple lower-order boundary treatment and we can focus on wall and outflow boundary treatments. For the solid wall, we use a lower-order fixed wall boundary treatment based on [5]. That is, we first do a local characteristic decomposition based on $\boldsymbol{U}_{\text{near}}$. To improve readability, we use a simplified notation for the eigenvectors. Then,

$$U_1 = \frac{(V_{\text{near}})_1}{l_{11} + l_{14}\frac{RT_{\text{wall}}}{\gamma-1}}, \tag{14}$$

$$U_2 = 0, \quad U_3 = 0, \quad U_4 = \frac{U_1 RT_{\text{wall}}}{\gamma - 1}. \tag{15}$$

We remark that (14) is valid for the lower boundaries of Fig. 1a and 1b, and left boundary of Fig. 1b. For the right boundary,

$$U_1 = \frac{(V_{\text{near}})_4}{l_{41} + l_{44}\frac{RT_{\text{wall}}}{\gamma-1}}. \tag{16}$$

After updating the conservative variables, we compute the convective part of the convex combination, $\boldsymbol{V}_{ccc} = \boldsymbol{L}\boldsymbol{U}$. This strategy is valid for the convective terms. For the diffusive terms we also do a local decomposition with $\boldsymbol{U}_{\text{near}}$ [5]

$$\boldsymbol{V}_d = \boldsymbol{L}_d \boldsymbol{U}_{\text{near}}. \tag{17}$$

Then,

$$(U_d)_1 = \frac{(V_d)_1}{l_{d11} + l_{d14}\frac{RT_{\text{wall}}}{\gamma-1}}, \tag{18}$$

$$(U_d)_2 = 0, \quad (U_d)_3 = 0, \quad (U_d)_4 = \frac{(U_d)_1 RT_{\text{wall}}}{\gamma - 1}, \tag{19}$$

$$\boldsymbol{V}_{ccd} = \boldsymbol{L}\boldsymbol{U}_d. \tag{20}$$

We combine convective and diffusive contributions through a convex combination [15]

$$\boldsymbol{V} = \boldsymbol{\alpha}\boldsymbol{V}_{ccc} + (1 - \boldsymbol{\alpha})\boldsymbol{V}_{ccd}, \tag{21}$$

with $\boldsymbol{\alpha} = \operatorname{diag}(\alpha_1, \alpha_2, \alpha_3, \alpha_4)$, [5, 15]

$$\alpha_r = \frac{b_r}{b_r + \epsilon_r}, \tag{22}$$

$$b_r = \left(B_{r1}^2 + B_{r2}^2 + B_{r3}^2 + B_{r4}^2\right)\Delta x^2, \quad r = 1, 3, 4, \tag{23}$$

$$b_2 = \frac{1}{3}\left(b_1 + b_3 + b_4\right), \tag{24}$$

$$\epsilon_r = 9(\lambda_d)_r^2, \quad \text{for } r = 2, 3, 4, \tag{25}$$

$$\epsilon_1 = 3\left[(\lambda_d)_2^2 + (\lambda_d)_3^2 + (\lambda_d)_4^2\right], \tag{26}$$

$$\boldsymbol{B} = \boldsymbol{L}_d \boldsymbol{F}'(\boldsymbol{U})\boldsymbol{R}_d = \begin{bmatrix} u & 0 & -\frac{a}{\gamma} & 0 \\ 0 & u & 0 & 0 \\ -a & 0 & u & -a \\ 0 & 0 & -\frac{a}{\gamma}(\gamma - 1) & u \end{bmatrix}. \tag{27}$$

Then, we have at the boundary

$$\boldsymbol{U}_{i,j} = \boldsymbol{R}\boldsymbol{V}, \tag{28}$$

for a fixed i or j.

We described the simplest albeit lower-order wall boundary treatment based on [5]. Regarding that inflow and upper boundaries are lower order, this wall boundary treatment will be enough.

For the Navier–Stokes equations, the number of boundary conditions to be imposed depends on the boundary [20]. For an outflow, we shall impose three boundary conditions for the diffusive terms. For the inviscid terms, the number of boundary conditions follows the Euler equations strategy. If the outflow is supersonic, we shall impose no boundary conditions, which can be easily done with extrapolation. However, we need more information for a subsonic outflow and the diffusive terms. This information is usually available

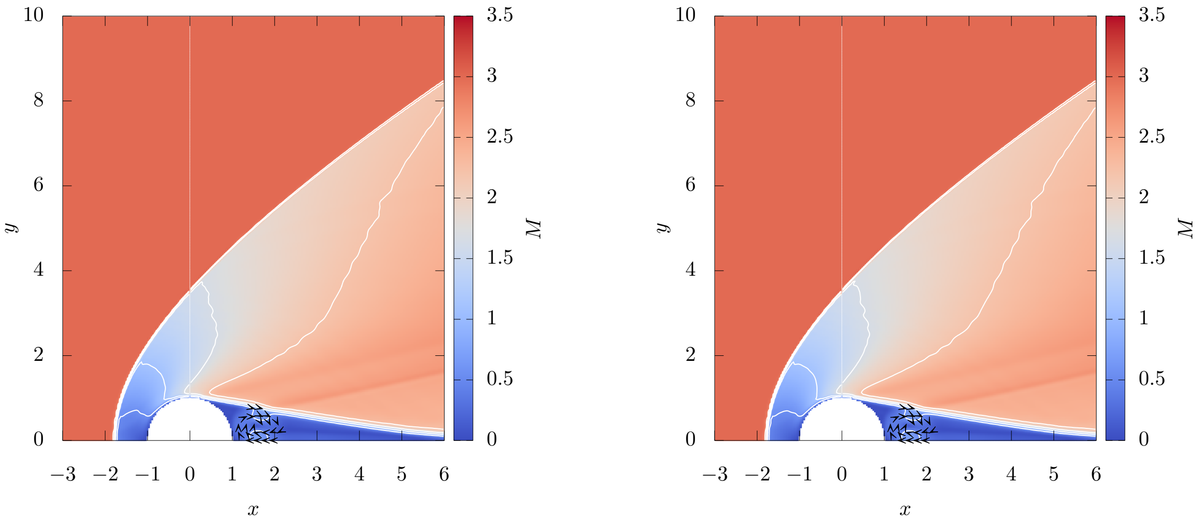

(a) Far-field

(b) Riemann solver

Figure 2: Mach number color map and contours from 0 to 3 every 0.55 for the cylinder flow with $\Delta x = 3/80$ and $t_f = 0.2\ s$.

through the far-field boundary treatment. We use the non-reflecting far-field treatment of [14] and [12]

$$Ri^-_\infty = u_\infty - \frac{2}{\gamma - 1}a_\infty, \quad Ri^+_{\text{near}} = u_{\text{near}} - \frac{2}{\gamma - 1}a_{\text{near}}, \tag{29}$$

$$u = \frac{Ri^-_\infty + Ri^+_{\text{near}}}{2}, \quad v = v_{\text{near}} + (u - u_{\text{near}}), \tag{30}$$

$$a = \frac{\gamma - 1}{4}\left(Ri^-_\infty + Ri^+_{\text{near}}\right), \tag{31}$$

$$\rho = \left(\frac{\rho^\gamma_{\text{near}} a^2}{\gamma p_{\text{near}}}\right)^{1/\gamma - 1}, \tag{32}$$

$$p = \frac{\rho a^2}{\gamma}. \tag{33}$$

Then, we compute the conservative variables and use them at the ghost points for $i = N_x + 1, \dots, N_x + 3$ and a fixed j.

Now, we change how the primitive variables are obtained at the boundary. We use the nearest point as the left state, $\boldsymbol{W}_L$, and use the free-stream data as the right state, $\boldsymbol{W}_R$. Then, we employ Numerica's exact Riemann solver to compute the intermediary state, $\boldsymbol{W}$ [30].

We show the Mach number color map, contours, and recirculation for the flow past a cylinder with **$\Delta x = 3/80$, $t_f = 2\ s$, the far-field, and** the exact Riemann solver boundary treatments in Fig. 2. We also show the Mach number profile at the symmetry line ($y = 0$) in Fig. 3. Both boundary treatments show similar behavior. Furthermore, the characteristic boundary also share similarities with the exact Riemann solver.

3. The ILW outflow boundary treatment

Inspired by our previous analysis, one could propose a high-order and -resolution ILW procedure using the exact Riemann solver. However, we do not see it in interior schemes because of the cost. Several alternatives to the exact Riemann solver are available, e.g., approximate Riemann solvers. Here, we employ the characteristic boundary condition, which is a common building block for the ILW procedure.

Suppose we want to impose the boundary conditions at the outflow of Fig. 4. We need an average state to perform a local characteristic decomposition. Following the same idea as before, we need to assess the eigenvalues signs to correctly impose the boundary conditions.

Since we have an outflow, there are two possibilities $u - a < 0$ and $u - a \geq 0$ for convective terms. For $u - a < 0$, we shall impose one boundary condition

$$(V_{ccc})_1 = (V_\infty)_1, \tag{34}$$

and $(V_{ccc})_m$ for $m = 2, 3, 4$ are computed with an WENO-type extrapolation. Otherwise, all $\boldsymbol{V}_{ccc}$ components are computed with an WENO-type extrapolation.

With $\boldsymbol{V}_{ccc}$ one could proceed as in Section 2 and impose lower-order boundary conditions. Here, we take a step further and propose a high-order and -resolution boundary treatment. We begin describing a new WENO-type extrapolation. Consider the smoothness indicators [26, 28, 10, 16]

$$\beta_r = \sum_{l=1}^{r} \Delta x^{2l-1} \int_a^b \left(\frac{d^l}{dx^l} q(x)\right)^2 dx \quad r = 1, \dots, 4. \tag{35}$$

The smoothness indicator for WENO-type extrapolations is not computed for the smaller stencil, $r = 0$, since it is a constant approximation. **Usually, it depends on mesh**

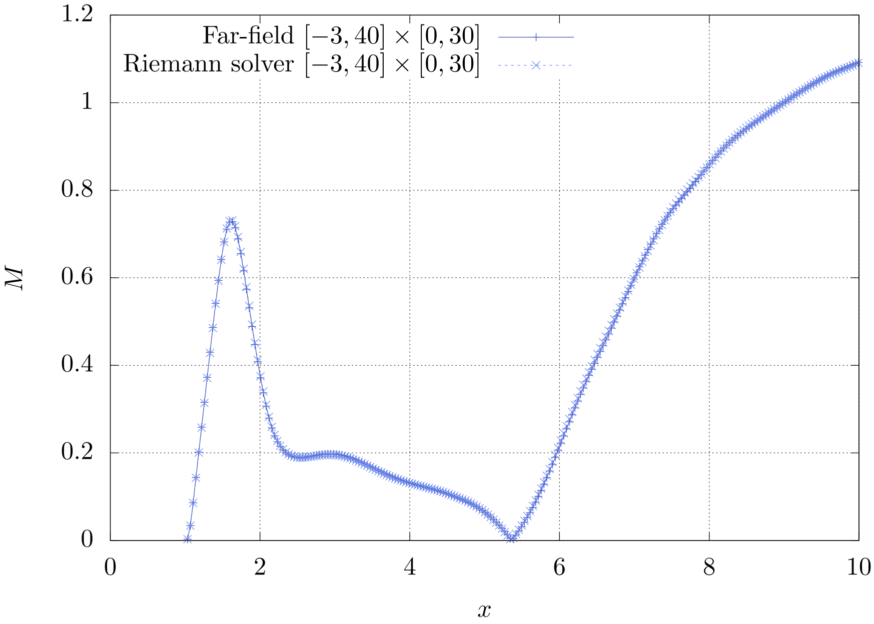

Figure 3: Mach number profile at the symmetry line for the cylinder flow with $\Delta x = 3/80$ and $t_f = 0.2$ s.

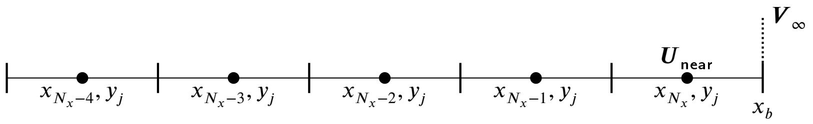

Figure 4: Outflow boundary.

size or other stencils. This is a challenge for determining how smooth the stencils. Also, we will approximate values away from the stencils, e.g., at the ghost points. First, let us assess the smoothness indicators for approximating values far away from the stencils, say $b \to \infty$. Since $q(x)$ are usually Lagrange polynomials, $\beta_r \to \infty$. Therefore, we propose $a = x_{N-1/2}$ and $b = x_{N+7/2}$.

We expect that b will increase the β_r magnitude for smooth and non-smooth stencils. Then, we can remove the dependency on smaller stencil smoothness indicators through the following non-linear weights

$$\omega_r = \exp(-\beta_r^p), \quad r = 1, \dots, 4, \tag{36}$$

where $p > 1$ is a power parameter and even.

We remark that $\omega_r \to 1$ if $\beta_r \to 0$ and $\omega_r \to 0$ if $\beta_r \to \infty$. One advantage of the WENO-Z$^+$ of [1] is that the weight of less-smooth substencils are increased to improve the resolution at smooth waves. In our case, if the substencil is smooth enough $\omega_r > 0$, it will contribute to the approximation, and increase the resolution in a similar way.

The resulting approximation is

$$s(x) = p_0 + \sum_{r=1}^{4} \omega_r p_r(x), \tag{37}$$

with

$$p_0 = q_0, \quad p_r(x) = q_r(x) - q_{r-1}(x), \quad r = 1, \dots, 4. \tag{38}$$

For comparison purpose, we show the new WENO-type extrapolation and the one of Tan et al. (2012) [28] in Fig. 5 for a $\Delta x = 2/320$ mesh. The problem is an 1D Euler flow with $[-1,1]$ as domain and

$$\rho(x) = \begin{cases} 1.1(x+0.5)+0.3 & \text{if } -0.5 \le x \le 0, \\ 0.3 & \text{otherwise}, \end{cases} \tag{39}$$
$$u(x) = 1, \quad p(x) = 2,$$

as initial condition. The analytical solution is a translation of the initial condition. We set the final time in a way that there is one point after the shock. This a severe test case and the new WENO-type extrapolation performed slightly better than Tan et al., as the last point is more close to the analytical solution. Furthermore, the dependencies on mesh size and other stencils were removed.

Now, we return to the boundary treatment. We already have $\partial_x^{(k)}\{\boldsymbol{V}_{ccc}\}_{k=0}^{4}$ at the boundary. For the convective terms, if $u - a \ge 0$ we shall impose no boundary condition. Otherwise, with the ILW we update [15, 16, 5]

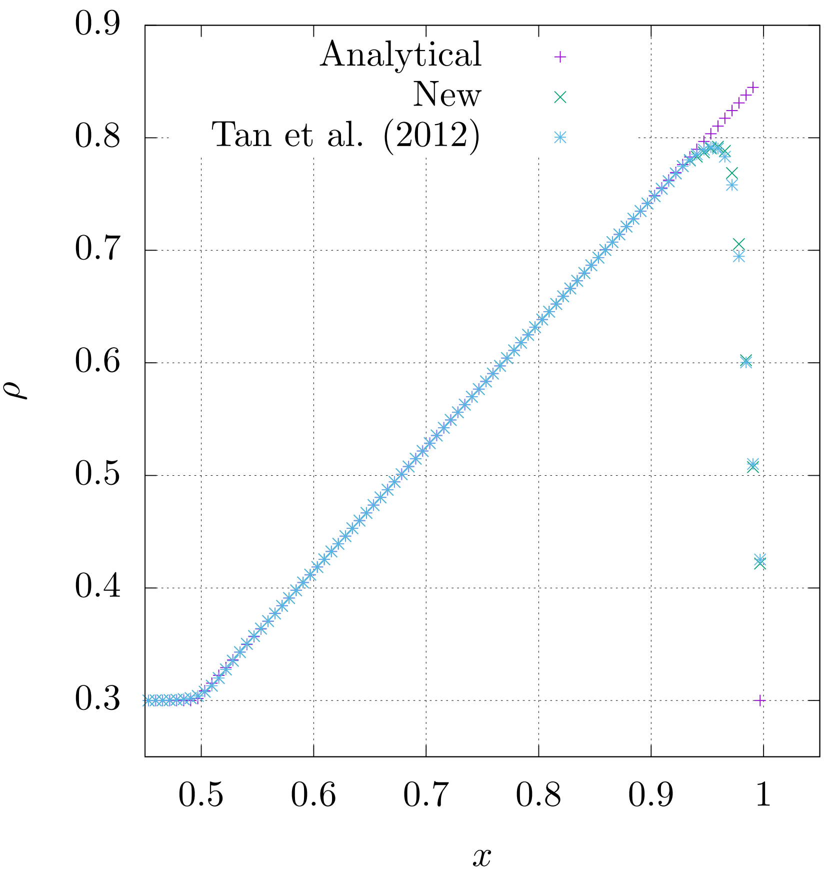

Figure 5: Density for the 1D Euler flow with $\Delta x = 2/320$.

$$\partial_x^{(1)}(V_{ccc})_1 = \frac{-(U_1)_t - (G_1)_y - r_{12}u_b\partial_x^{(1)}(V_{ccc})_2}{r_{11}(u_b - a_{rb})} - \frac{r_{13}u_b\partial_x^{(1)}(V_{ccc})_3 + r_{14}(u_b + a_{rb})\partial_x^{(1)}(V_{ccc})_4}{r_{11}(u_b - a_{rb})}. \tag{40}$$

As in [5], the $\boldsymbol{U}_t$ are zero because we impose steady boundary conditions. We still need approximations to the fluxes, $\boldsymbol{F}(\boldsymbol{U})$ and $\boldsymbol{G}(\boldsymbol{U})$, and the viscous terms, $\boldsymbol{S}_1$ and $\boldsymbol{S}_2$, derivatives. Similarly as in [5], we propose to compute $\boldsymbol{V}$ in the vicinity of x_b and use it to obtain 2D least squares polynomials, P_r, with $r = 1, \dots, 4$. This, because the high magnitude of the pressure can cause difficulties with the least squares and extrapolation. Then, we can approximate $\boldsymbol{V}_y$ and $\boldsymbol{V}_{yy}$ on different substencils [16, 5]. For instance,

$$S_0 = \{0\}, \quad S_1 = \{P_1(x_{N_x-1}, y_j)_y, P_1(x_{N_x}, y_j)_y\}, \tag{41}$$

$$S_2 = \{P_2(x_{N_x-2}, y_j)_y, P_2(x_{N_x-1}, y_j)_y, P_2(x_{N_x}, y_j)_y\}, \tag{42}$$

$$S_3 = \{P_3(x_{N_x-3}, y_j)_y, P_3(x_{N_x-2}, y_j)_y, \tag{43}$$

$$P_3(x_{N_x-1}, y_j)_y, P_3(x_{N_x}, y_j)_y\}, \tag{44}$$

$$S_4 = \{P_4(x_{N_x-4}, y_j)_y, P_4(x_{N_x-3}, y_j)_y, \tag{45}$$

$$P_4(x_{N_x-2}, y_j)_y, P_4(x_{N_x-1}, y_j)_y, P_4(x_{N_x}, y_j)_y\}. \tag{46}$$

Then, we use the WENO-type extrapolation to obtain $\partial_x^{(k)}\{\boldsymbol{V}_y\}_{k=0}^1$ and $\partial_x^{(0)}\boldsymbol{V}_{yy}$ at the boundary. Now, we can compute $\boldsymbol{U}$, $\boldsymbol{U}_x$, $\boldsymbol{U}_y$, $\boldsymbol{U}_{xy}$, $\boldsymbol{U}_{yy}$, and the remaining terms at the boundary [5]

$$\boldsymbol{G}(\boldsymbol{U})_y = \boldsymbol{G}'(\boldsymbol{U})\boldsymbol{U}_y, \ \boldsymbol{F}(\boldsymbol{U})_x = \boldsymbol{F}'(\boldsymbol{U})\boldsymbol{U}_x, \tag{47}$$

$$\boldsymbol{S}_{1x} = \boldsymbol{\psi}_1 \frac{\partial \boldsymbol{W}}{\partial \boldsymbol{U}} \boldsymbol{U}_{xy} + \boldsymbol{\psi}_2 \frac{\partial \boldsymbol{W}}{\partial \boldsymbol{U}} \boldsymbol{U}_{xx} + \boldsymbol{N}_1, \tag{48}$$

$$\boldsymbol{S}_{2y} = \boldsymbol{\psi}_3 \frac{\partial \boldsymbol{W}}{\partial \boldsymbol{U}} \boldsymbol{U}_{xy} + \boldsymbol{\psi}_4 \frac{\partial \boldsymbol{W}}{\partial \boldsymbol{U}} \boldsymbol{U}_{yy} + \boldsymbol{N}_2, \tag{49}$$

where the formulae for $\boldsymbol{\psi}_1$, $\partial \boldsymbol{W}/\partial \boldsymbol{U}$, $\boldsymbol{\psi}_2$, $\boldsymbol{N}_1$, $\boldsymbol{\psi}_3$, $\boldsymbol{\psi}_4$, and $\boldsymbol{N}_2$ can be found in the Appendix.

For the diffusive terms, we use $\boldsymbol{U}_{\text{avg}}$ to perform a decomposition and a WENO-type extrapolation to obtain $\partial_x^{(k)}\{\boldsymbol{V}_d\}_{k=0}^4$ at the boundary. Then,

$$\boldsymbol{V}_{d\infty} = \boldsymbol{L}_d \boldsymbol{U}_\infty, \tag{50}$$

$$\partial_x^{(0)}(V_d)_m = (V_{d\infty})_m, \quad m = 2,3,4. \tag{51}$$

With the ILW and Appendix formulae, we update [15, 16, 5]

$$\begin{aligned} \boldsymbol{l}_{d1}\partial_x^{(2)}\boldsymbol{U}_d &= \partial_x^{(2)}(V_d)_1, \\ \Psi_{1m}\partial_x^{(2)}\boldsymbol{U}_d &= (U_m)_t + F_m(\boldsymbol{U})_x + G_m(\boldsymbol{U})_y - \\ &\Psi_{2m}\boldsymbol{U}_{yy} - \Psi_{3m}\boldsymbol{U}_{xy} - N_m, m = 2,3,4, \end{aligned} \tag{52}$$

$$\partial_x^{(k)}\boldsymbol{U}_d = \boldsymbol{R}_d\partial_x^{(k)}\boldsymbol{V}_d, \quad k = 0,1,3,4. \tag{53}$$

Here, we take

$$\partial_x^{(k)}\{\boldsymbol{V}_{ccd}\}_{k=0}^4 = \boldsymbol{L}\partial_x^{(k)}\{\boldsymbol{U}_d\}_{k=0}^4, \tag{54}$$

and the convex combination is

$$\partial_x^{(k)}\{\boldsymbol{V}\}_{k=0}^4 = \boldsymbol{\alpha}\partial_x^{(k)}\{\boldsymbol{V}_{ccc}\}_{k=0}^4 + (1-\boldsymbol{\alpha})\partial_x^{(k)}\{\boldsymbol{V}_{ccd}\}_{k=0}^4. \tag{55}$$

With a Taylor expansion, we compute $\boldsymbol{V}$, $\boldsymbol{V}_x$, and $\boldsymbol{V}_y$ at the ghost points for a fixed j, e.g.,

$$\begin{aligned} \boldsymbol{V}_{i,j} &= \sum_{k=0}^{4} \frac{(x_{i,j} - x_b)^k}{k!}\partial_x^{(k)}\boldsymbol{V}, \\ (\boldsymbol{V}_x)_{i,j} &= \sum_{k=0}^{3} \frac{(x_{i,j} - x_b)^k}{k!}\partial_x^{(k+1)}\boldsymbol{V}. \end{aligned} \tag{56}$$

Then,

$$\boldsymbol{U} = \boldsymbol{R}\boldsymbol{V}, \quad \boldsymbol{U}_x = \boldsymbol{R}\boldsymbol{V}_x, \quad \boldsymbol{U}_y = \boldsymbol{R}\boldsymbol{V}_y, \tag{57}$$

$$\boldsymbol{W}_x = \frac{\partial \boldsymbol{W}}{\partial \boldsymbol{U}}\boldsymbol{U}_x, \quad \boldsymbol{W}_y = \frac{\partial \boldsymbol{W}}{\partial \boldsymbol{U}}\boldsymbol{U}_y, \tag{58}$$

and $\boldsymbol{F}(\boldsymbol{U})$ and $\boldsymbol{S}_1$ can be computed at the ghost points.

Our interior scheme demands $\boldsymbol{U}$, $\boldsymbol{F}(\boldsymbol{U})$, and $\boldsymbol{S}_1$ at the ghost points. Therefore, the ILW outflow boundary treatment is complete.

4. Numerical problems

4.1. Smooth test case

We first solve a smooth test case for checking the **new WENO-type extrapolation and** the ILW outflow boundary treatment **accuracies**. The steady-state analytical solution is [5, 16]

$$\begin{aligned} \rho(x,y) &= \left(\frac{11}{10}\right)^{\sin(x)\cos(y)}, \quad u(x,y) = 200 + 2(x^2 - \pi^2), \\ v(x,y) &= 100 + (y^2 - \pi^2), \quad p(x,y) = 101325. \end{aligned} \tag{59}$$

We insert (59) in the Navier–Stokes equations and obtain four source terms. Using the source terms in the discretized equations, the Navier–Stokes will be analytically satisfied.

For this problem, the analytical solution is known. Therefore, $\boldsymbol{U}_{\text{avg}}$ is replaced by the analytical solution at the boundary. The accuracy analysis is shown in Tab. 1, where one can see the convergence towards the designed order.

4.2. Flow past a cylinder

We revisit the supersonic airflow past a cylinder to test our ILW outflow boundary treatment. The initial estimate is [5, 15]

$$\begin{aligned} M(x,y) &= \begin{cases} x^2 + y^2 - 1, & \text{if } 1 < x^2 + y^2 \le M_\infty + 1, \\ M_\infty, & \text{otherwise,} \end{cases} \\ \rho(x,y) &= \rho_0\left(1 + \frac{\gamma-1}{2}M^2\right)^{-1/(\gamma-1)}, \\ p(x,y) &= p_0\left(1 + \frac{\gamma-1}{2}M^2\right)^{-\gamma/(\gamma-1)}, \\ u(x,y) &= Ma, \quad v = 0, \end{aligned} \tag{60}$$

where the cylinder radius is one and ρ_0 and p_0 are computed with free-stream data: $T_\infty = 800\ K$, $p_\infty = 101.325\ kPa$ and $M_\infty = 3$. The gas constant, specific heat ratio, Prandtl number, and viscosity were obtained with CoolProp library and based on free-stream data [4].

The Mach number color map **for $\Delta x = 3/80$** is shown in Fig. 6, where one can see that the oblique shock, wake region, and the recirculation are well captured. We also compare the Mach number profile at the symmetry line for the far-field, Riemann solver, and ILW boundary treatments in Fig. 7. The ILW profile is similar to the other boundary **treatments in extended domains. However, the far-field boundary treatment in a small domain shows different behavior than other solutions.**

We remark that the domain size is significantly small for the ILW outflow boundary treatment. However, one should respect the phenomena and speed regime. For example, the flow is subsonic for $x \lesssim 9$. If the right domain is smaller than that, $\boldsymbol{V}_\infty$ will not be a good approximation and the outflow will not behave as in Fig. 7. On other hand, if the domain is bigger, the boundary treatment will handle subsonic regions when marching from the initial estimate.

4.3. NACA 0012 airfoil

To compare the ILW outflow boundary treatment with more practical applications, we solved nitrogen flows around a NACA 0012 airfoil and compared the results with experimental data of [13]. The free-stream data is $T_\infty = 200.2967\ K$, $M_\infty = 0.3018$, and $p_\infty \approx 366.37\ kPa$ [13]. The first test has an angle of attack of 0 °, $c = 0.1524\ m$ chord length, and $[-c, 2c] \times [-c, c]$ as domain. For simplicity, we use constant viscosity and lower-order boundary treatment for inflow, wall, lower, and upper boundaries. At the wall, we impose an adiabatic condition using the nearest point to it. The right boundary is handled by the ILW outflow boundary treatment. The Mach number color map, contours, and pressure coefficient **for $\Delta x \approx 4.94 \times 10^{-4}\ m$** are shown in Fig. 8.

Although our boundary treatment is steady, solving the Navier–Stokes equations can result in transient solutions. Furthermore, this type of equations can be sensitive to the initial condition. In this work, we employed an Euler

$\Delta x = \Delta y$	L^1 norm	Order	L^2 norm	Order	L^∞ norm	Order
$2\pi/10$	$6.57E-04$	–	$8.18E-04$	–	$1.85E-03$	–
$2\pi/20$	$2.46E-05$	4.74	$2.97E-05$	4.79	$6.36E-05$	4.87
$2\pi/40$	$7.93E-07$	4.95	$9.74E-07$	4.93	$2.35E-06$	4.75
$2\pi/80$	$2.46E-08$	5.01	$3.06E-08$	4.99	$7.64E-08$	4.95
$2\pi/160$	$7.65E-10$	5.01	$9.55E-10$	5.00	$2.39E-09$	5.00

Table 1
Density L^1, L^2, and L^∞ norms and orders for the smooth test case.

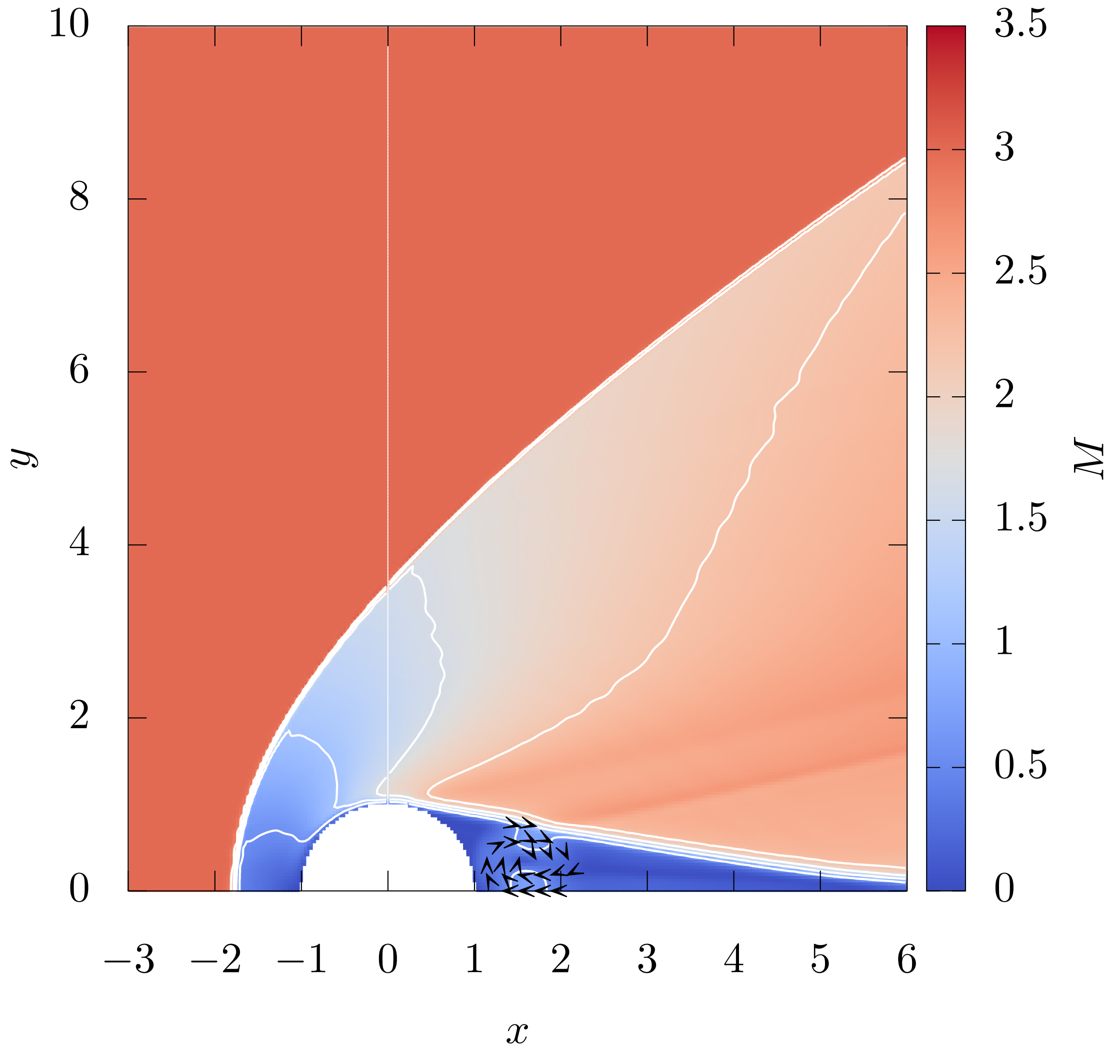

Figure 6: Mach number color map, contours from 0 to 3 every 0.55, and recirculation for the cylinder flow with $\Delta x = 3/80$ and $t_f = 0.2$ s.

solution initial guess. The Euler solver was first-order everywhere with adiabatic and no-slip conditions at the walls. The Navier–Stokes simulation time is showed for reference.

In the color maps, we can see that the symmetry is preserved until a certain time, even with the WENO multi-resolution good hold of symmetry [36, 5]. The symmetry break impacts the pressure coefficient, flow properties, and unsteady structures. The symmetry break could be caused by, e.g., floating-point errors [11]. For the pressure coefficient, it causes the upper and lower pressure coefficients to behave differently, as we can see in Fig. 8d. We can also see that the numerical solution is far from the experimental data at certain regions. This may happen because the mesh is not fine enough near the wall, the wall boundary treatment is only first order, and/or the viscous effects are overestimated. The boundary layer thickness appears to be bigger than it

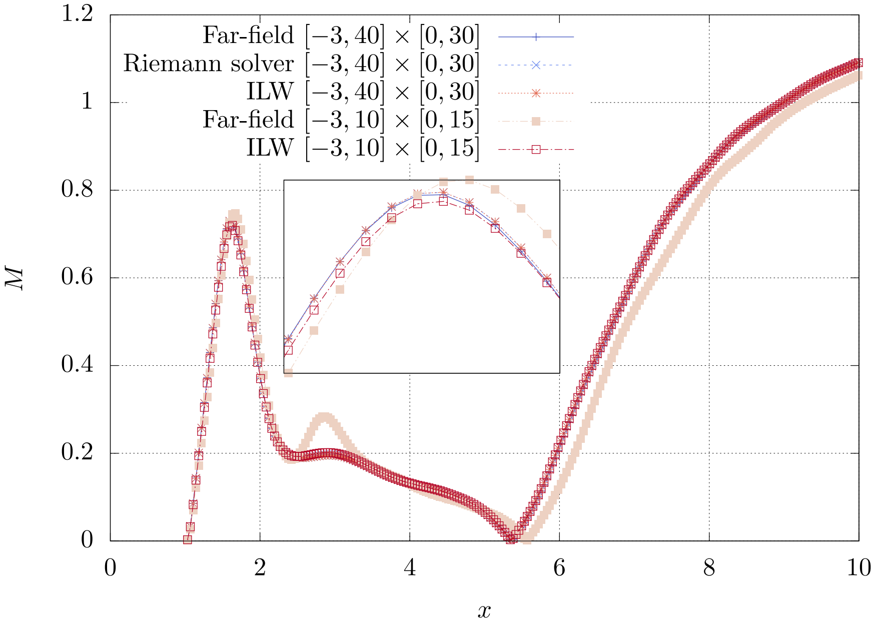

Figure 7: Mach number profile at the symmetry line for the cylinder flow with $\Delta x = 3/80$ and $t_f = 0.2\ s$.

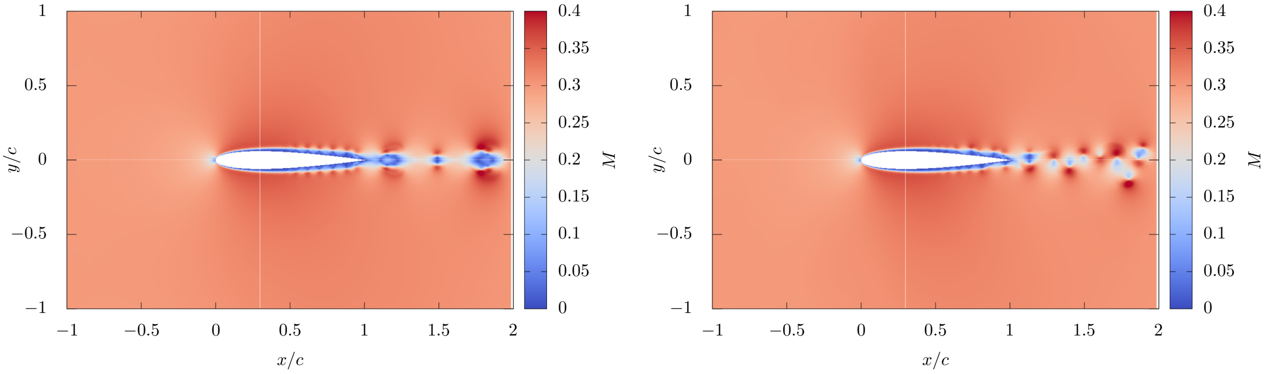

(a) $t_f = 0.0098\ s$.

(b) $t_f = 0.04\ s$.

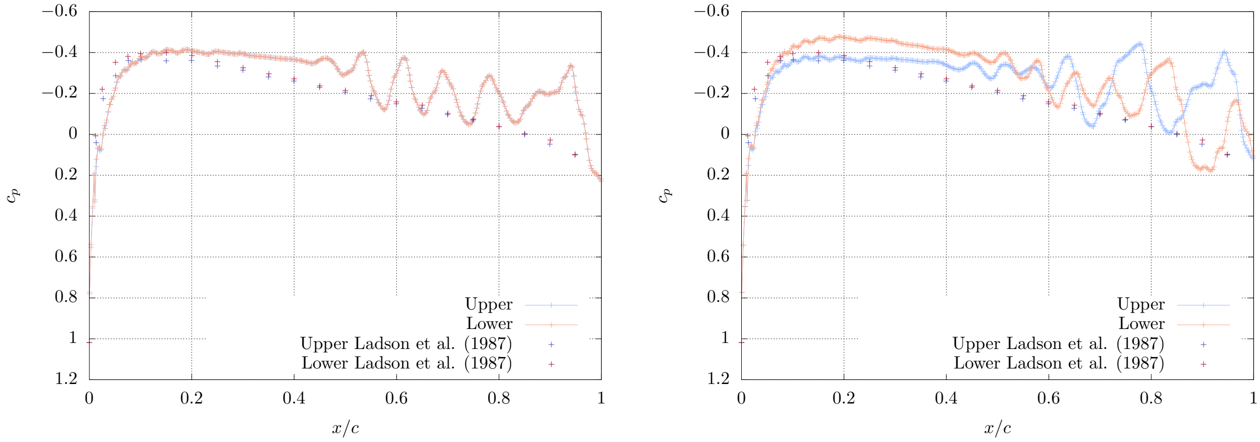

(c) $t_f = 0.0098\ s$.

(d) $t_f = 0.04\ s$.

Figure 8: Mach number color maps and contours from 0 to 0.4 every 0.05 and pressure coefficients for the NACA 0012 airfoil at 0 ° angle of attack with $\Delta x \approx 4.94 \times 10^{-4}\ m$.

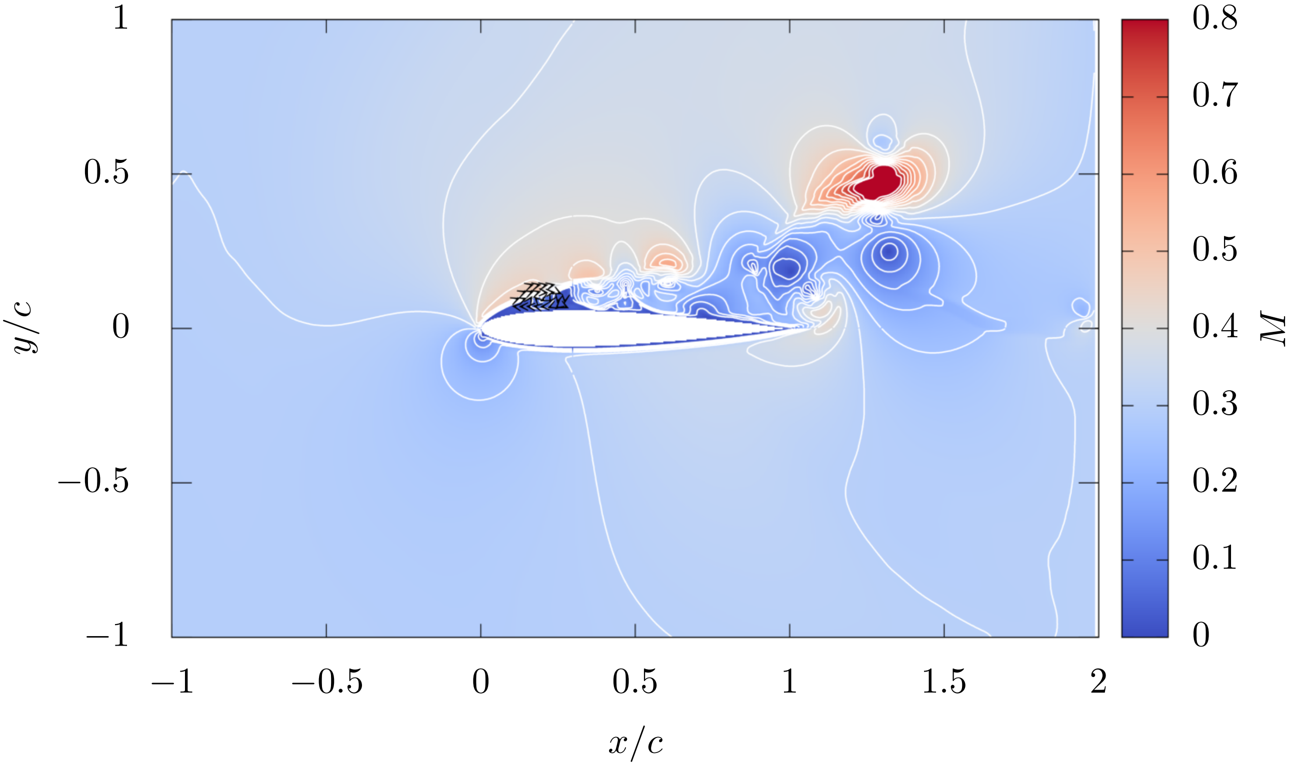

Figure 9: Mach number color maps and contours from 0 to 0.8 every 0.05 for the NACA 0012 airfoil at 12.026 ° angle of attack with $\Delta x \approx 4.94 \times 10^{-4}\ m$ and $t_f = 0.0286\ s$.

should. Especially, for the mid to end airfoil region. These can also be explained by the absence of a turbulence model.

We also solve the same airfoil problem at 12.026 ° angle of attack [13]. Now, the upper boundary is also handled by the ILW outflow boundary treatment and the computational domain is $[-c, 2c] \times [-2c, c]$. For this particular analysis, we have an interesting unsteady phenomenon known as a separation bubble [31, 22]. The Mach number color map, contours, and pressure coefficient **for $\Delta x = 4.94 \times 10^{-4}$** are shown in Fig. 9 and 10.

We can see a recirculation near the leading edge at the upper surface in Fig. 9. This gives rise to unsteady phenomena. In [22], the authors refer to the unsteady phenomena as Kelvin–Helmholtz instabilities and von Kármán vortices. We can also see how the instabilities affect the pressure coefficient and a certain distance from experimental data. As stated in [17], even RANS can overpredict the lift and drag at post-stall angles of attack. Despite these preliminary results being promising, further analysis and methods are needed to improve the agreement with experimental data.

4.4. NACA 9520 cascade flow

Our final numerical problem is also a preliminary result for a practical application. The cascade flow is often solved when studying turbine blades. Cold and hot airflow around the VKI LS-94 turbine blade is a common CFD analysis [24, 32, 8, 7]. For simplicity, we employ a 280 mm chord NACA 9520 profile rotated 36 ° and spaced 0.2 m horizontally. The total temperature and pressure are 772 K and 470 kPa [8]. At the outflow, the Mach number is set to 0.79 [8]. The computational domain is $[0.1, C_{ax} + 0.1] \times [-0.175, 0.025]$, where C_{ax} is the axial chord length. Flow parameters and other properties are computed with CoolProp library and total properties [4]. The viscosity and Prandtl number are constant.

At the inflow, $\boldsymbol{W}_0 = (p_0/(RT_0), 0, 0, p_0)^T$ and we employ a first-order characteristic boundary treatment. The upper and lower boundaries are periodic and we again use first-order adiabatic wall boundary treatment. For the outflow, we employ the ILW outflow boundary treatment with $\boldsymbol{W}_2$. For a viscous flow, the friction will change the total pressure. However, for our preliminary analysis, it is enough

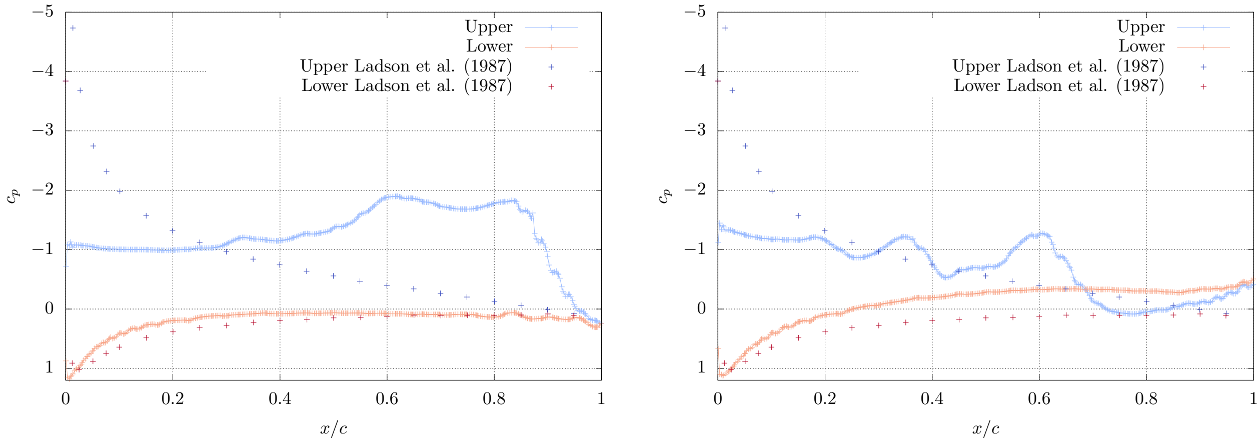

(a) $t_f = 0.0098$ s.

(b) $t_f = 0.0286$ s.

Figure 10: Pressure coefficients for the NACA 0012 airfoil at 12.026 ° angle of attack with $\Delta x \approx 4.94 \times 10^{-4}$ m.

to approximate pressure and temperature through gas dynamics relations

$$T_2 = T_0 \left[1 + \frac{(\gamma - 1)}{2} M_2^2\right]^{-1}, \qquad p_2 = p_0 \left[1 + \frac{(\gamma - 1)}{2} M_2^2\right]^{-\gamma/(\gamma-1)}. \tag{61}$$

The density is obtained from the equation of state and the velocity is approximated as

$$u = M_2 a_2 \cos(36\,°), \quad v = -M_2 a_2 \sin(36\,°). \tag{62}$$

$\boldsymbol{W}_2$ is then used to compute $\boldsymbol{V}_\infty$ in the ILW outflow boundary treatment. From former discussions, we remark that $\boldsymbol{V}_\infty$ is an approximate state which will be partially used to impose the boundary conditions. In fact, most of the information will come from interior points. Therefore, this does not mean that the resulting velocity vector will have the same direction as $\boldsymbol{W}_2$.

The Mach number color map and contours are shown in Fig. 11 **for $\boldsymbol{\Delta x = 5.01 \times 10^{-4}}$**. We can see similarities in the wake region and vortices with common cascade analysis [24, 32, 8, 18, 2].

As in the NACA 0012 flows, one can still improve the solution. For instance, with better mesh discretization, high-order wall boundary treatment, and turbulence modeling. Issues regarding the cascade flow modeling are not rare [19, 24]. As stated in [24], difficulties regarding grid convergence for URANS, hard-to-satisfy DES, DDES, and LES requirements, and deviations from experiments may happen in cascade flows. The authors also commented that there is room for more experimental analysis in this type of flow. Therefore, we can also expect the numerical cascade flow as an active field of research.

5. Concluding remarks

The far-field boundary treatment is a class of popular and robust strategies. While providing well-posedness these strategies can help reducing the domain size. In some of these strategies, Riemann invariants are employed and they are similar to Riemann solvers. The boundary treatment success also depends on the extrapolation and variable types.

We showed similarities between a far-field, exact Riemann solver, and ILW boundary treatments. Also, we proposed and tested an ILW strategy for imposing high-order and -resolution outflow boundary conditions and an WENO-type extrapolation. The ILW boundary treatment provides a good representation of the flow features near the boundary, it is well-posed, allows small domains, and can handle flows with high-magnitude properties.

Through a smooth test case, we showed that our strategy is high-order. In the supersonic flow past a cylinder, one can see that the oblique shock is well captured and our strategy has high resolution. The domain size can be reduced without any problem when marching to steady state. However, the speed regime and flow phenomena must be respected or a better approximation to the characteristic variables should be employed.

In the NACA 0012 and NACA 9520 flows, we showed a good representation of unsteady phenomena. For instance, vortices, separation bubble, and wake region. In light of that, the numerical methods employed in this work are promising for solving practical CFD applications. Although sharing issues with other methods, their accuracy still needs to be improved. This can be done by refining the mesh near the airfoil surface, high-order wall boundary treatment, and turbulence modeling.

6. Declaration of Interests

The authors report no conflict of interest.

A. Matrices and vectors for the ILW

For completeness, the required matrices and vectors for computing the ILW outflow boundary treatment are shown

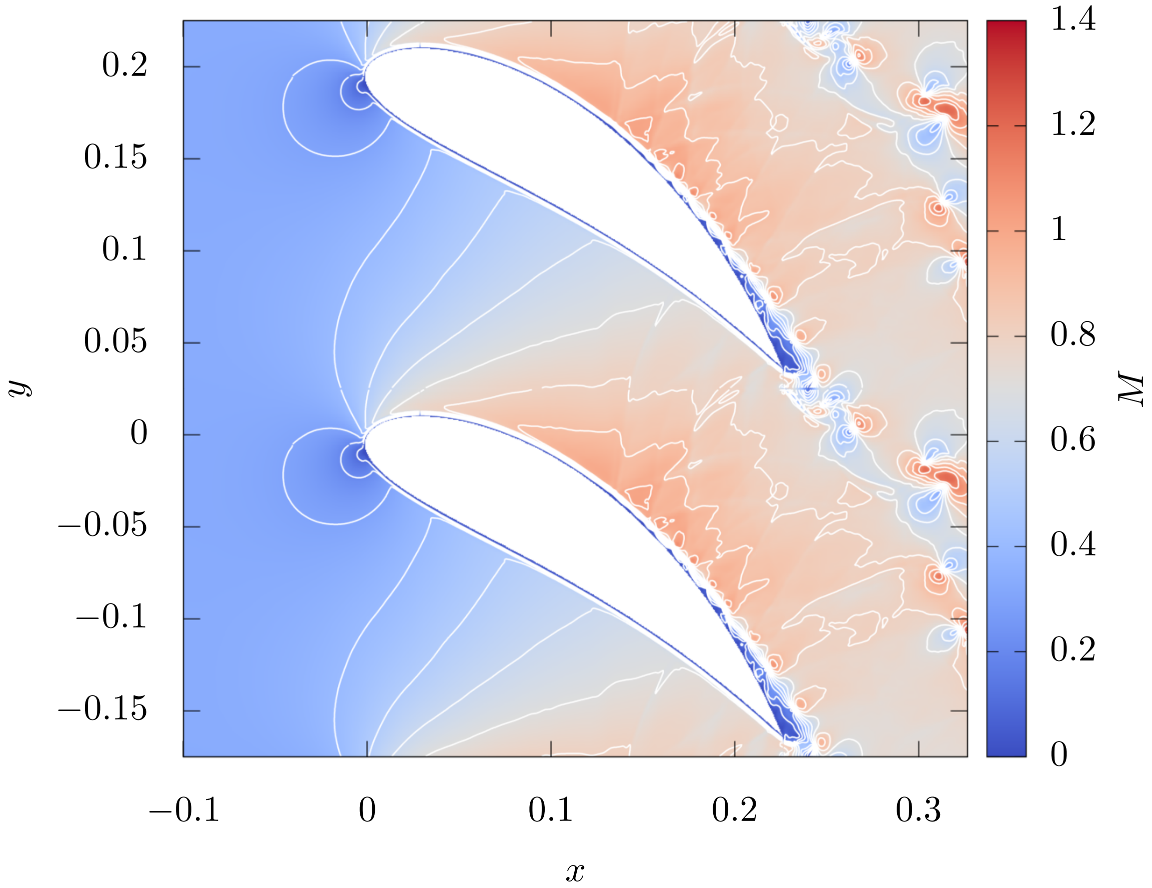

Figure 11: Mach number color maps and contours from 0 to 1.4 every 0.1 for the cascade flow with $\Delta x \approx 5.01 \times 10^{-4}$ m and $t_f = 0.04$ s.

next [5]

$$\boldsymbol{\psi_1} = \begin{bmatrix} 0 & 0 & 0 & 0 \\ 0 & 0 & -2\mu/3 & 0 \\ 0 & \mu & 0 & 0 \\ 0 & \mu v & -2\mu u/3 & 0 \end{bmatrix}, \tag{63}$$

$$\boldsymbol{\psi_2} = \begin{bmatrix} 0 & 0 & 0 & 0 \\ 0 & 4\mu/3 & 0 & 0 \\ 0 & 0 & \mu & 0 \\ -\mu a^2/[\rho Pr(\gamma-1)] & 4\mu u/3 & \mu v & \mu\gamma/[\rho Pr(\gamma-1)] \end{bmatrix}, \tag{64}$$

$$\boldsymbol{\psi_3} = \begin{bmatrix} 0 & 0 & 0 & 0 \\ 0 & 0 & \mu & 0 \\ 0 & -2\mu/3 & 0 & 0 \\ 0 & -2\mu v/3 & \mu u & 0 \end{bmatrix}, \tag{65}$$

$$\boldsymbol{\psi_4} = \begin{bmatrix} 0 & 0 & 0 & 0 \\ 0 & \mu & 0 & 0 \\ 0 & 0 & 4\mu/3 & 0 \\ -\mu a^2/[\rho Pr(\gamma-1)] & \mu u & 4\mu v/3 & \mu\gamma/[\rho Pr(\gamma-1)] \end{bmatrix}, \tag{66}$$

$$\begin{gathered} (N_{w1})_1 = 0, \\ (N_{w1})_2 = \mu_x \left(\frac{4}{3}u_x - \frac{2}{3}v_y\right), \\ (N_{w1})_3 = \mu_x \left(u_y + v_x\right), \\ (N_{w1})_4 = u_x\mu \left(\frac{4}{3}u_x - \frac{2}{3}v_y\right) + v_x\mu\left(u_y + v_x\right) + \\ \left(\frac{\mu\gamma}{Pr(\gamma-1)}\right)_x \left(\frac{p}{\rho}\right)_x + u\mu_x\left(\frac{4}{3}u_x - \frac{2}{3}v_y\right) + \\ v\mu_x\left(u_y + v_x\right) + \frac{\mu\gamma}{Pr(\gamma-1)}\left(\frac{2p\rho_x^2}{\rho^3} - \frac{2p_x\rho_x}{\rho^2}\right), \end{gathered} \tag{67}$$

$$\begin{gathered}
(N_{w2})_1 = 0, \\
(N_{w2})_2 = \mu_y \left(u_y + v_x\right), \\
(N_{w2})_3 = \mu_y \left(\frac{4}{3}v_y - \frac{2}{3}u_x\right), \\
(N_{w2})_4 = u_y\mu \left(u_y + v_x\right) + v_y\mu \left(\frac{4}{3}v_y - \frac{2}{3}u_x\right) + \\
\left(\frac{\mu\gamma}{Pr(\gamma - 1)}\right)_y \left(\frac{p}{\rho}\right)_y + u\mu_y \left(u_y + v_x\right) + \\
v\mu_y \left(\frac{4}{3}v_y - \frac{2}{3}u_x\right) + \frac{\mu\gamma}{Pr(\gamma - 1)} \left(\frac{2p\rho_y^2}{\rho^3} - \frac{2p_y\rho_y}{\rho^2}\right).
\end{gathered} \tag{68}$$

$$\boldsymbol{M} = \begin{bmatrix} 0 & 0 & 0 & 0 \\ \dfrac{\rho_x u - \rho u_x}{\rho^2} & -\dfrac{\rho_x}{\rho^2} & 0 & 0 \\ \dfrac{\rho_x v - \rho v_x}{\rho^2} & 0 & -\dfrac{\rho_x}{\rho^2} & 0 \\ \left(uu_x + vv_x\right)(\gamma - 1) & -u_x(\gamma - 1) & -v_x(\gamma - 1) & 0 \end{bmatrix},$$
$$\boldsymbol{O} = \begin{bmatrix} 0 & 0 & 0 & 0 \\ \dfrac{\rho_y u - \rho u_y}{\rho^2} & -\dfrac{\rho_y}{\rho^2} & 0 & 0 \\ \dfrac{\rho_y v - \rho v_y}{\rho^2} & 0 & -\dfrac{\rho_y}{\rho^2} & 0 \\ \left(uu_y + vv_y\right)(\gamma - 1) & -u_y(\gamma - 1) & -v_y(\gamma - 1) & 0 \end{bmatrix}. \tag{69}$$

$$\begin{aligned}
&\boldsymbol{N_1} = \boldsymbol{\psi_1 M U}_y + \boldsymbol{\psi_2 M U}_x + \boldsymbol{N_{w1}}, \\
&\boldsymbol{N_2} = \boldsymbol{\psi_3 O U}_x + \boldsymbol{\psi_4 O U}_y + \boldsymbol{N_{w2}}.
\end{aligned} \tag{70}$$

$$\boldsymbol{\Psi_1} = \boldsymbol{\psi_2}\frac{\partial \boldsymbol{W}}{\partial \boldsymbol{U}}, \tag{71}$$

$$\boldsymbol{\Psi_2} = \boldsymbol{\psi_4}\frac{\partial \boldsymbol{W}}{\partial \boldsymbol{U}}, \tag{72}$$

$$\boldsymbol{\Psi_3} = \boldsymbol{\psi_1}\frac{\partial \boldsymbol{W}}{\partial \boldsymbol{U}} + \boldsymbol{\psi_3}\frac{\partial \boldsymbol{W}}{\partial \boldsymbol{U}}, \tag{73}$$

$$\boldsymbol{N} = \boldsymbol{N_1} + \boldsymbol{N_2}. \tag{74}$$

$$\frac{\partial \boldsymbol{W}}{\partial \boldsymbol{U}} = \begin{bmatrix} 1 & 0 & 0 & 0 \\ -u/\rho & 1/\rho & 0 & 0 \\ -v/\rho & 0 & 1/\rho & 0 \\ \frac{1}{2}(\gamma - 1)(u^2 + v^2) & (1 - \gamma)u & (1 - \gamma)v & \gamma - 1 \end{bmatrix}. \tag{75}$$

References

[1] Acker, F., Borges, R.B.R., Costa, B., 2016. An improved WENO-Z scheme. Journal of Computational Physics 313, 726–753. doi:https://doi.org/10.1016/j.jcp.2016.01.038.

[2] Arnone, A., Pacciani, R., 1997. Numerical prediction of trailing edge wake shedding. doi:10.1115/97-GT-089. v001T03A020.

[3] Bayliss, A., Turkel, E., 1982. Far field boundary conditions for compressible flows. Journal of Computational Physics 48, 182–199. doi:https://doi.org/10.1016/0021-9991(82)90046-8.

[4] Bell, I.H., Wronski, J., Quoilin, S., Lemort, V., 2014. Pure and pseudo-pure fluid thermophysical property evaluation and the open-source thermophysical property library coolprop. Industrial & Engineering Chemistry Research 53, 2498–2508. doi:10.1021/ie4033999.

[5] Borges, R.B.de R., da Silva, N.D.P., Gomes, F.A.A., Shu, C.W., 2021a. High-resolution viscous terms discretization and ilw solid wall boundary treatment for the navier-stokes equations. Archives of Computational Methods in Engineering doi:https://doi.org/10.1007/s11831-021-09657-9.

[6] Borges, R.B.de R., da Silva, N.D.P., Gomes, F.A.A., Shu, C.W., Tan, S., 2021b. A sequel of inverse lax-wendroff high order wall boundary treatment for conservation laws. Archives of Computational Methods in Engineering doi:https://doi.org/10.1007/s11831-020-09454-w.

[7] Cicatelli, G., Sieverding, C.H., 1996. The effect of vortex shedding on the unsteady pressure distribution around the trailing edge of a turbine blade. doi:10.1115/96-GT-359. v001T01A091.

[8] El-Gendi, M.M., Doi, K., Ibrahim, M.K., Mori, K., Nakamura, Y., 2010. Comparison between hot and cold flow conditions of turbine cascade. Transactions of the Japan Society for Aeronautical and Space Sciences 53, 171–179. doi:10.2322/tjsass.53.171.

[9] Engquist, B., Halpern, L., 1988. Far field boundary conditions for computation over long time. Applied Numerical Mathematics 4, 21–45. doi:https://doi.org/10.1016/S0168-9274(88)80004-7.

[10] Filbet, F., Yang, C., 2013. An inverse lax–wendroff method for boundary conditions applied to boltzmann type models. Journal of Computational Physics 245, 43 – 61. doi:https://doi.org/10.1016/j.jcp.2013.03.015.

[11] Fleischmann, N., Adami, S., Adams, N.A., 2019. Numerical symmetry-preserving techniques for low-dissipation shock-capturing schemes. Computers & Fluids 189, 94 – 107. doi:https://doi.org/10.1016/j.compfluid.2019.04.004.

[12] Junqueira-Junior, C., Azevedo, J.L.F., Scalabrin, L.C., Basso, E., 2013. A study of physical and numerical effects of dissipation on turbulent flow simulations. Journal of Aerospace Technology and Management 5, 145–168. doi:http://dx.doi.org/10.5028/jatm.v5i2.179.

[13] Ladson, C.L., Hill, A.S., G.Johnson Jr., W., 1987. Pressure Distributions from High Reynolds Number Transonic Tests of an NACA 0012 Airfoil in the Langley 0.3-Meter Transonic Cryogenic Tunnel. NASA Technical Memorandum. NASA.

[14] Long, L.N., Khan, M.M.S., Sharp, H.T., 1991. Massively parallel three-dimensional euler/navier–stokes method. AIAA Journal 29, 657–666. doi:https://doi.org/10.2514/3.10635.

[15] Lu, J., Fang, J., Tan, S., Shu, C.W., Zhang, M., 2016. Inverse Lax–Wendroff procedure for numerical boundary conditions of convection–diffusion equations. Journal of Computational Physics 317, 276 – 300. doi:https://doi.org/10.1016/j.jcp.2016.04.059.

[16] Lu, J., Shu, C.W., Tan, S., Zhang, M., 2020. An inverse Lax–Wendroff procedure for hyperbolic conservation laws with changing wind direction on the boundary. Journal of Computational Physics , 109940doi:https://doi.org/10.1016/j.jcp.2020.109940.

[17] Mitchell, S., Ogbonna, I., Volkov, K., 2021. Aerodynamic characteristics of a single airfoil for vertical axis wind turbine blades and performance prediction of wind turbines. Fluids 6. doi:10.3390/fluids6070257.

[18] Mokulys, T., Congiu, F., Rose, M.G., Abhari, R.S., 2009. Unsteady numerical investigation of the effect of wakes with eddy shedding in different axial turbine aerofoils. Proceedings of the Institution of Mechanical Engineers, Part A: Journal of Power and Energy 223, 1001–1016. doi:10.1243/09576509JPE787.

[19] Ning, W., He, L., 2001. Some modeling issues on trailing-edge vortex shedding. AIAA Journal 39, 787–793. doi:10.2514/2.1411.

[20] Nordström, J., Svärd, M., 2005. Well-posed boundary conditions for the navier–stokes equations. SIAM Journal on Numerical Analysis 43, 1231–1255. doi:https://doi.org/10.1137/040604972.

[21] Riahi, H., Constant, E., Favier, J., Meliga, P., Serre, E., Meldi, M., Goncalves da Silva, E., 2017. Direct Numerical Simulation Of Compressible Flows Aroundspherical Bodies Using The Immersed

Boundary Method, in: Direct and Large-Eddy Simulation, Pisa, Italy.

[22] Rodríguez, I., Lehmkuhl, O., Borrell, R., Oliva, A., 2013. Direct numerical simulation of a naca0012 in full stall. International Journal of Heat and Fluid Flow 43, 194–203. doi:`https://doi.org/10.1016/j.ijheatfluidflow.2013.05.002`. 7th International Symposium on Turbulence Heat & Mass Transfer (THMT-7), Palermo Conference on Modelling Fluid Flow (CMFF'12).

[23] Shu, C.W., 1998. Essentially non-oscillatory and weighted essentially non-oscillatory schemes for hyperbolic conservation laws. Springer Berlin Heidelberg, Berlin, Heidelberg. pp. 325–432. URL: `http://dx.doi.org/10.1007/BFb0096355`, doi:`10.1007/BFb0096355`.

[24] Sieverding, C., Manna, M., 2020. A review on turbine trailing edge flow. International Journal of Turbomachinery, Propulsion and Power 5. doi:`10.3390/ijtpp5020010`.

[25] Svärd, M., Carpenter, M.H., Nordström, J., 2007. A stable high-order finite difference scheme for the compressible navier–stokes equations, far-field boundary conditions. Journal of Computational Physics 225, 1020–1038. doi:`https://doi.org/10.1016/j.jcp.2007.01.023`.

[26] Tan, S., Shu, C.W., 2010. Inverse Lax-Wendroff procedure for numerical boundary conditions of conservation laws. Journal of Computational Physics 229, 8144–8166.

[27] Tan, S., Shu, C.W., 2011. A high order moving boundary treatment for compressible inviscid flows. Journal of Computational Physics 230, 6023 – 6036. doi:`https://doi.org/10.1016/j.jcp.2011.04.011`.

[28] Tan, S., Wang, C., Shu, C.W., Ning, J., 2012. Efficient implementation of high order inverse Lax–Wendroff boundary treatment for conservation laws. Journal of Computational Physics 231, 2510–2527. doi:`https://doi.org/10.1016/j.jcp.2011.11.037`.

[29] Thomas, J.L., Salas, M.D., 1986. Far-field boundary conditions for transonic lifting solutions to theeuler equations. AIAA Journal 24, 1074–1080. doi:`https://doi.org/10.2514/3.9394`.

[30] Toro, E.F., 2009. Riemann Solvers and Numerical Methods for Fluid Dynamics: A Practical Introduction. 3 ed., Springer Berlin Heidelberg.

[31] van Dyken, R.D., 1997. Experimental and computational analysis of separation bubble behavior for compressible, steady and oscillatory flows over a NACA 0012 airfoil at M=0.3 and a reynolds number of 540,000. Ph.D. thesis. URL: `https://calhoun.nps.edu/handle/10945/8365`.

[32] Wang, S., Wen, F., Zhang, S., Zhang, S., Zhou, X., 2019. Influences of trailing boundary layer velocity profiles on wake vortex formation in a high-subsonic-turbine cascade. Proceedings of the Institution of Mechanical Engineers, Part A: Journal of Power and Energy 233, 186–198. doi:`10.1177/0957650918779935`.

[33] Wubs, F.W., Boerstoel, J.W., Van Der Wees, A.J., 1984. Grid-size reduction in flow calculations on infinite domains by higher-order far-field asymptotics in numerical boundary conditions. Journal of Engineering Mathematics 18, 157–177. doi:`https://doi.org/10.1007/BF00042733`.

[34] Yuan, R., Zhong, C., 2018. An immersed-boundary method for compressible viscous flows and its application in the gas-kinetic bgk scheme. Applied Mathematical Modelling 55, 417–446. doi:`https://doi.org/10.1016/j.apm.2017.10.003`.

[35] Zhang, X., Shu, C.W., 2012. Positivity-preserving high order finite difference WENO schemes for compressible Euler equations. Journal of Computational Physics 231, 2245 – 2258. doi:`https://doi.org/10.1016/j.jcp.2011.11.020`.

[36] Zhu, J., Shu, C.W., 2018. A new type of multi-resolution weno schemes with increasingly higher order of accuracy. Journal of Computational Physics 375, 659 – 683. doi:`https://doi.org/10.1016/j.jcp.2018.09.003`.